*Supporting Information*

**Ligand Design and Nuclearity Variation towards Dual Emissive Pt(II) Complexes for Singlet Oxygen Generation, Dual Channel Bioimaging, and Theranostics**

Marsel Z. Shafikov,*[a,b] Alfiya F. Suleymanova,[c] Roger J. Kutta[a], Aleksander Gorski[d], Aleksandra Kowalczyk[e], Magdalena Gapińska[f], Konrad Kowalski[g], Rafał Czerwieniec*[a]

[a]*Institut für Physikalische und Theoretische Chemie, Universität Regensburg, Universitätsstrasse 31, Regensburg, D-93053, Germany.*

[b]*Ural Federal University, Mira 19, Ekaterinburg, 620002, Russia.*

[c]*Chemistry Department, University of York, Heslington, York, YO10 5DD, UK*

[d]*Institute of Physical Chemistry, Polish Academy of Sciences, Kasprzaka 44/52, Warsaw, Poland*

[e]*Department of Molecular Microbiology, Faculty of Biology and Environmental Protection, University of Łódź, Banacha 12/16, 90-237, Łódź, Poland.*

[f]*Laboratory of Microscopic Imaging and Specialized Biological Techniques, Faculty of Biology and Environmental Protection, University of Łódź, Banacha 12/16, 90-237, Łódź, Poland.*

[g]*Faculty of Chemistry, Department of Organic Chemistry, University of Łódź, Tamka 12, 91-403 Łódź, Poland.*

**Synthesis and chemical characterization.**

**General**

NMR spectra were recorded on a Bruker AVANCE III HD 400 spectrometer, operating at 400 MHz for ^{1}H nuclei and at 376 MHz for ^{19}F nuclei, with residual protic solvent used as internal standard. Elemental analysis was carried out on ELEMENTAR vario MICRO CUBE instrument at central analytical services of the University of Regensburg. Mass-spectroscopy (FD-MS) was performed on a JEOL AccuTOF GCX instrument at the central analytical services of the University of Regensburg.

**Synthetic procedures and characterizations**

*2,5-bis(5-(trifluoromethyl)pyridin-2-yl)thiophene* (proligand **H₂L**). 2,5-bis(trimethylstannyl)thiophene (1.000 g, 2.44 mmol), 2-bromo-5-(trifluoromethyl)pyridine (1.103 g, 4.88 mmol) and dimethylformamide (50 mL) were put in a Schlenk's flask which then was sealed with a rubber seal. The flask was then deaerated by three-fold subsequent application of vacuum and argon lines. Then tetrakis(triphenylphosphine)palladium(0) 10 mol-% (0.282 g) was added quickly and the deaeration procedure was repeated. The flask was heated at 100°C in an oil bath for 12 hours and then cooled down to

ambient temperature. Then 50 mL of cold water were added to the solution, the formed precipitate was filtered, washed with water and methanol subsequently, and dried under vacuum. Yield 76% (0.7 g). ^{1}H NMR (CDCl$_3$, 400 MHz): δH 8.85 (s, 2H), 7.95 (dd, 2H, J = 8.31, J=2.13 Hz), 7.79 (d, 2H, J=8.31). 7.75 (s, 2H) ^{19}F NMR (CDCl$_3$, 400 MHz): δF -62.86.

Synthesis of *Pt(tfbpH)(acac)* (**Pt-1**) *and Pt$_2$(tfbp)(acac)$_2$* (**Pt-2**). The proligand **H$_2$L** (0.300 g, 0.801 mmol) was put in a flask with 50 mL of acetic acid under argon and heated to 120°C in an oil bath. Then K$_2$PtCl$_4$ (0.665 g, 1.603 mmol) dissolved in 1 mL of water was added. Then the oil bath was let to cool down to 80°C and flask was heated for 48 hours with stirring. The flask was cooled to ambient temperature and the formed precipitate of dichlorobridged Pt(II) complex was filtered, washed with water and methanol successively and dried under vacuum. Sodium acetylacetonate (acac) (11.820 g, 8.015 mmol) and the dried dichloro-bridged Pt(II) complex were put into a flask with 50 mL of acetone. The flask was equipped with condenser and heated at reflux for 24 hours. The solvent then was removed *in vacuo* and 50 mL dichloromethane (CH$_2$Cl$_2$) were added to the flask. The precipitate was filtered and washed with 100 mL of dichloromethane. The combined filtrate was collected and concentrated to *ca.* 5 mL. Purification by chromatography (silica gel, CH$_2$Cl$_2$) allowed to isolate pure mono-nuclear Pt(II) complex **Pt-1** with 30% yield and pure di-nuclear Pt(II) complex (**Pt-2**) with 7% yield.

Characterization of **Pt-1.**

^{1}H NMR (CD$_2$Cl$_2$, 400 MHz): δH 9.15 (s, 1H), δH 8.82 (s, 1H), 7.96 (m, 3H), 7.72 (s, 1H), 7.47 (d, 2H, J=8.45 Hz), 5.58 (s, 1H), 2.06 (s, 3H), 2.05(s, 3H). ^{19}F NMR (CD$_2$Cl$_2$, 400 MHz): δF -62.57, -62.58.

Field desorption mass-spectrometry (FD-MS): calculated for [M]$^+$ (C$_{21}$H$_{14}$F$_6$N$_2$O$_2$PtS) 667.0324, found 666.9820.

Elemental analysis: calculated C 37.79, H 2.11, N 4.40%; found C 37.74, H 2.05, N 4.10%.

Characterization of **Pt-2.**

^{1}H NMR (CDCl$_3$, 400 MHz): δH 9.18 (s, 2H), 7.90 (d, 2H, J=8.49), 7.90 (d, 2H, J=8.49, J=1.82), 7.38 (d, 2H, J=8.49 Hz), 5.46 (s, 2H), 2.02 (s, 6H), 1.84(s, 6H). ^{19}F NMR (CDCl$_3$, 400 MHz): δF -62.82.

Field desorption mass-spectrometry (FD-MS): calculated for [M]$^+$ (C$_{26}$H$_{20}$F$_6$N$_2$O$_4$Pt$_2$S) 960.0189, found 960.0330.

Elemental analysis: calculated C 32.51, H 2.10, N 2.92%; found C 32.62, H 2.10, N 2.86%.

**Single crystal x-ray diffraction analysis**

*Experimental for complex **Pt-1**.* Single clear brown plate-shaped crystals were obtained by convectional diffusion of methanol into solution of complex **Pt-1** in dichloromethane. A suitable crystal 0.20×0.13×0.05 mm$^3$ was selected and mounted on a MITIGEN holder oil on a SuperNova, Single source at offset, Atlas diffractometer. The crystal was kept at a steady $T = 123.01(10)$ K during data collection. The structure was

solved with the ShelXT[1] structure solution program using the Intrinsic Phasing solution method and by using Olex2[2] as the graphical interface. The model was refined with version 2016/6 of ShelXL[1] using Least Squares minimisation.

*Experimental for complex* **Pt-2**. Single clear brown plate-shaped crystals were obtained by convectional diffusion of methanol into solution of complex **Pt-2** in dichloromethane. A suitable crystal $0.12{\times}0.09{\times}0.05$ mm$^3$ was selected and mounted on a MITIGEN holder oil on a SuperNova, Single source at offset, Atlas diffractometer. The crystal was kept at a steady $T = 123.01(10)$ K during data collection. The structure was solved with the ShelXT[1] structure solution program using the Intrinsic Phasing solution method and by using Olex2[2] as the graphical interface. The model was refined with version 2018/3 of ShelXL[1] using Least Squares minimisation.

**Table S1.** Crystallographic data for complexes **Pt-1** and **Pt-2**

| Crystallographic parameter | Pt-1 | Pt-2 |
|---|---|---|
| CCDC deposition number | 2050225 | 2050226 |
| Formula | $C_{21}H_{14}F_6N_2O_2PtS$ | $C_{26}H_{20}F_6N_2O_4Pt_2S$ |
| $D_{calc.}$/ g cm$^{-3}$ | 2.092 | 2.378 |
| $\mu$/mm$^{-1}$ | 14.009 | 20.667 |
| Formula Weight | 667.49 | 960.68 |
| Colour | clear brown | clear brown |
| Shape | plate | plate |
| Size/mm$^3$ | 0.20×0.13×0.05 | 0.12×0.09×0.05 |
| $T$/K | 123.01(10) | 123.01(10) |
| Crystal System | monoclinic | monoclinic |
| Space Group | $P2_1/c$ | $I2/a$ |
| $a$/Å | 14.64944(18) | 23.1553(3) |
| $b$/Å | 17.61184(20) | 10.26130(10) |
| $c$/Å | 8.54712(12) | 22.6419(3) |
| $\alpha$/° | 90 | 90 |
| $\beta$/° | 106.0760(14) | 93.8390(10) |
| $\gamma$/° | 90 | 90 |
| $V$/Å$^3$ | 2118.96(5) | 5367.72(11) |
| $Z$ | 4 | 8 |
| $Z'$ | 1 | 1 |
| Wavelength/Å | 1.54184 | 1.54184 |
| Radiation type | CuK$_\alpha$ | CuK$_\alpha$ |
| $\Theta_{min}$/° | 4.020 | 3.827 |
| $\Theta_{max}$/° | 74.323 | 76.419 |
| Measured Refl. | 25871 | 40213 |
| Independent Refl. | 4290 | 5620 |
| Reflections Used | 4147 | 5307 |
| $R_{int}$ | 0.0246 | 0.0449 |
| Parameters | 358 | 488 |
| Restraints | 142 | 330 |
| Largest Peak | 0.678 | 1.566 |
| Deepest Hole | -0.616 | -1.021 |
| GooF | 1.076 | 1.056 |
| $wR_2$ (all data) | 0.0441 | 0.0652 |
| $wR_2$ | 0.0437 | 0.0637 |
| $R_1$ (all data) | 0.0182 | 0.0265 |
| $R_1$ | 0.0175 | 0.0246 |

**Steady-state optical spectroscopy.** The steady state photophysical measurements were performed on solutions of complexes **Pt-1** and **Pt-2** in dichloromethane. The UV-Vis absorption spectra were measured with a Varian Cary 300 double beam spectrometer. The emission room temperature photoluminescence spectra were measured with a Horiba Jobin Yvon DUETTA steady-state fluorescence spectrometer. The excitation spectra were measured with a Horiba Jobin Yvon Fluorolog-3 steady-state fluorescence spectrometer. The emission decay times were measured with a Horiba Jobin Yvon Fluorolog-3 spectrometer, a PicoBright PB-375 pulsed diode laser ($\lambda_{exc}$ = 378 nm, pulse width 100 ps) used as the

excitation source, and the PL signal was detected with a cooled photomultiplier attached to a FAST ComTec multichannel scalar PCI card with a time resolution of 250 ps. The PL quantum yield was determined with a Hamamatsu C9920-02 system equipped with a Spectralon® integrating sphere.
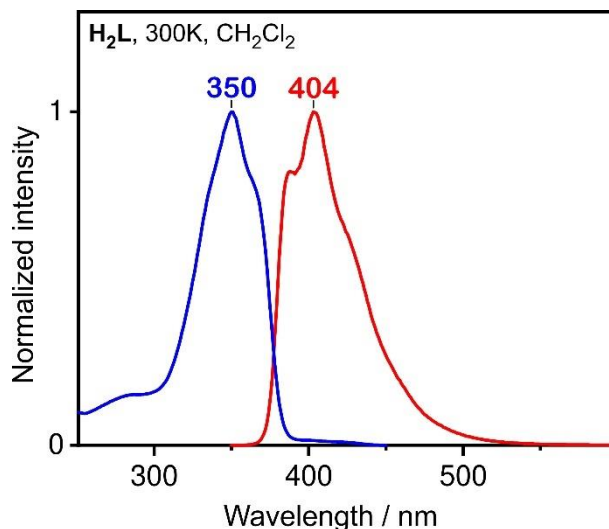


**Figure S1.** Absorption (blue) and emission (red) spectra of proligand **H₂L** in dichloromethane solution under ambient conditions.

## Singlet Oxygen Generation Studies.

Measurements of quantum efficiencies ($\phi_\Delta$) of singlet oxygen generation ($^1O_2$ ($^1\Delta_g$) emission at $\lambda_{max} = 1275$ nm) have been performed with a custom built highly sensitive experimental setup based on BENTHAM DTMc300 Double Monochromator and equipped with a TE Cooled PMT (Hamamatsu H10330C-75, 950–1700 nm registration range). A 405 nm continuous laser was used as photoexcitation source. The singlet oxygen quantum yield was determined by the relative method[3]. The efficiencies $\phi_\Delta$ were determined with respect to the well-known standard phenalenone ($\phi_\Delta = 0.96$ in dichloromethane at ambient temperature).[4] The accuracy in the estimation of singlet oxygen emission quantum yield was +/-10 %.

**Sub-ps Pump/Supercontinuum-Probe Spectroscopy.** The transient absorption in the UV/Vis with a typical time resolution of *ca.* 100 fs resolution on a time window up to 6.5 ns were recorded with the following in house build setup: A Ti:Sapphire oscillator-regenerative amplifier laser system (Coherent Libra) operating at a repetition rate of 1 kHz generating pulses at 800 nm with *ca.* 100 fs temporal pulse width and *ca.* 1.0 mJ energy per pulse is used as the fundamental source of the pump and probe pulses. About 60% of the fundamental energy are used to pump a collinear parametric amplifier (TOPAS-C, Light Conversion) for generating pump pulses to excite the sample into the $S_1 \leftarrow S_0$ absorption band, *i.e.* $\lambda_{exc} = 460$ nm for complex **1** and $\lambda_{exc} = 500$ nm for complex **2**. In each case the pulse energy was set to *ca.* 300 nJ

at the sample position focused to *ca.* 80 µm. About 1% of the fundamental 800 nm is used to generate a white-light supercontinuum (WLSC) by focusing the *ca.* 1 µJ of the 800 nm into a 5 mm thick $CaF_2$ disc that is rotated in an eccentric motion the keeping the orientation of the crystal axes relative to the polarization of the fundamental constant, and, thus, maintaining a linear polarization of the WLSC across the spectrum and over time. The residual 800 nm in the WLSC is strongly suppressed by passing through a thin high reflective 800 nm mirror balancing the spectral contribution around 800 nm to the rest of the WLSC. The WLSC is then split into a reference (25%) and signal beam path (75%). At the sample position the spot size of the probe pulse is *ca.* 40 µm. The signal and reference beams are spectrally dispersed by two in house build prism spectrographs and recorded with back-thinned full frame transfer (FFT) charged coupled device (CCD) cameras (3001 series; Ingineurbüro Stresing) which are triggered synchronously to the fundamental laser pulses. The combination of the FFT-CDD sensor (Hamamatsu, Sensor S7030-0906, 512 pixels) and the used optics provide a spectral resolution over the entire spectral range of $\pm50$ cm$^{-1}$, *i.e.,* $\pm0.5$ nm at 300 nm and $\pm2.5$ nm at 700 nm. The time delay between probe and pump is controlled via variation of the pump beam path using a 1 m delay stage (Zaber, X-LRT1000AL-AE53C-KX14NF) equipped with an open corner cube reflector. The sample solution was pumped continuously through a 1 mm quartz cell (Starna). Typically, the time axis is chosen to be linear from $-1$ ps up to 4.0 ps in 20 fs steps and logarithmic afterwards till the end of the delay stage of 6.5 ns with typically 400 time points. At each delay position of a scan an average over 200 transient absorption spectra were taken, each calculated for a baseline-corrected and referenced single shot. Averaging of at least five independent scans result in the final spectra. For recording the pure population dynamics of all excited states, the polarization between pump and probe pulses is set the magic angle (54.73°) *via* a λ/2 plate in the pump beam path. The averaged pre-t0 laser scatter signal was subtracted from the data and the *ca.* 2 ps chirp of the WLSC is corrected for prior to data analysis using the coherent artefact as an indicator for time zero at each wavelength. No smoothing or filtering procedures were applied to the data. The raw data are shown in Figure S2.
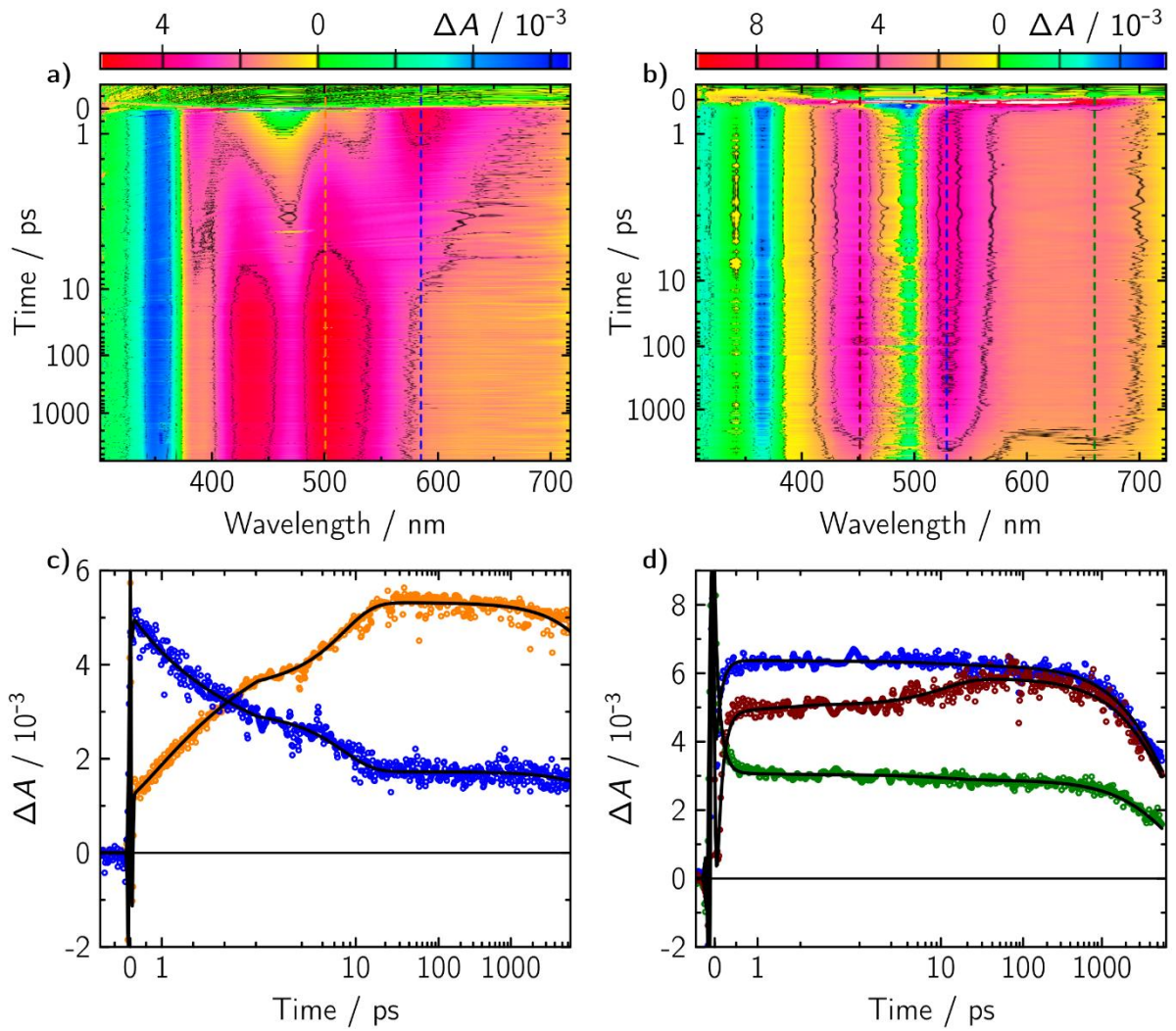
**Figure S2.** Transient absorption spectra in false color representation of complex **Pt-1** (**a**) and **Pt-2** (**b**) in CH$_2$Cl$_2$ when exciting into the corresponding S$_1 \leftarrow$ S$_0$ transition. **c** and **d** show selected time traces each along a certain probe wavelength as indicated by a dashed line in **a** and **b**, respectively. The black solid lines in **c** and **d** show the corresponding global fit to the data.

**Transient absorption data analysis and modelling.** Transient absorption data of single component systems are well analyzed by a global fit using an exponential ansatz. Here the global fits were performed using an in-house written program described previously.[5,6] As transient absorption data consist of a series of difference spectra recorded at a number of delay times, ΔA(t,λ), these may be represented as a rectangular matrix ΔA of dimension $N_T \times N_L$, in which each column is a time trace for a fixed wavelength of $N_T$ points, and each row is a spectrum at a given delay time of $N_L$ points. A global fit allows the decomposition of this matrix into a sum of products of one-dimensional functions, *i.e.*, a linear combination of products between spectra, $S_k(\lambda)$, and concentration-time profiles, $c_k(t)$, according to Eq. 1.

$$\Delta A_{ij} = \sum_{k=1}^{N} c_k(t_i) S_k(\lambda_j) = \sum_{k=1}^{N} c_{ik} S_{jk} \tag{1}$$

In Eq. 2 the raw data $\Delta A_{ij}$ are approximated by matrix **D**, in which the time profiles are represented as a linear combination of known analytic functions, $f_k(t)$:

$$D_{ij} = \sum_{k=1}^{N_C} c_k(t_i) S_k(\lambda_j) \tag{2}$$

$$c_k(t) = \sum_{k=1}^{N_F} f_l(t) X_{lk} \tag{3}$$

$N_C$ is the number of distinct spectral species and $N_F$ is the number of analytic functions describing the temporal behavior of a spectral species. Then, the model matrix **D** may be written as

$$\mathbf{D} = \mathbf{CS} = \mathbf{FXS} = \mathbf{FB} \tag{4}$$

Here, **C** is defined as a $N_T \times N_C$ matrix with elements, $C_{ik} = c_k(t_i)$, and **F** is defined as a $N_T \times N_C$ matrix with elements, $F_{il} = f_l(t_i)$. Consequently, the $k$-th row of the matrix **B**, with elements $B_{kj} = b_k(\lambda_j)$, represents the spectral changes associated with the time function, $f_k(t)$. With exponential decays (convoluted with the instrument response) as analytical function the corresponding spectra are called decay associated difference spectra (DADS). This representation allows to use efficient algorithms to solve the linear least squares problem

$$\chi^2 = \|\Delta\mathbf{A} - \mathbf{FB}\|^2 = \text{Min} \tag{5}$$

for given matrices $\Delta\mathbf{A}$ and **F**, while a nonlinear least squares algorithm is used for optimizing the rate constants in **F** so that at optimized $\chi^2$ the DADS and the corresponding rate constants are the unique result of the global fit not requiring any model for the kinetics involved in the transient processes. Only matrix **X** will contain all details of a model that may relate the actual species kinetics to the elementary function, $f_k(t)$, and, thus, can be chosen depending on the suggested underlying model alone. Then, the species associated spectra (SAS) in matrix **S** are calculated according to Eq. 6.

$$\mathbf{S} = \mathbf{X}^{-1}\mathbf{B} \tag{6}$$

Since the $\chi^2$ value found in the global fit does not change by the last step, all interpretation is performed with the same quality of fit.

***General kinetic model.*** Using the exponential ansatz, the analytic fitting function shown in Eq. 7 are used in the global lifetime analysis in order to determine the dynamics of each investigated compound

$$f_k(t) = \sum_{i=0}^{2} \frac{\mathrm{d}^i}{\mathrm{d}t^i} g_{\text{art}}(t - t_0) + \left( \delta(t) + \sum_{j=1}^{N} \exp(-\kappa_k t) \right) \otimes g_{\text{app}}(t - t_0) \tag{7}$$

Here, $\otimes\, g_{\text{app}}(t - t_0)$ means convolution with the apparatus function approximated by a Gaussian, $\delta(t)$ is the Dirac delta function, $\sum_{i=0}^{2} \frac{\mathrm{d}^i}{\mathrm{d}t^i} g_{\text{art}}(t - t_0)$ are a Gaussian and its first and second derivative with identical temporal widths allowing to account for the coherent artefact, and $N$ is the number of exponentials describing the dynamics of the TA change over time. The general photophysical processes including an intermediate hot triplet state can be described with the differential equations of Eq. 8.

$$\frac{\mathrm{d}}{\mathrm{d}t}\begin{pmatrix} [\,S_1\,] \\ [\,T_1^{\text{hot}}\,] \\ [\,T_1\,] \end{pmatrix} = -\begin{pmatrix} k_{\text{ic}} + k_{\text{r}} + k_{\text{isc}} & 0 & 0 \\ -k_{\text{isc}} & k_{\text{cool}} & 0 \\ 0 & -k_{\text{cool}} & k_{\text{bisc}} \end{pmatrix}\begin{pmatrix} [\,S_1\,] \\ [\,T_1^{\text{hot}}\,] \\ [\,T_1\,] \end{pmatrix} \tag{8}$$

The global fit absolutely determines the eigenvalues of the rate constant matrix are given in Eq. 8 which are

$$\kappa_1 = k_{\text{ic}} + k_{\text{r}} + k_{\text{isc}} \tag{9}$$

$$\kappa_2 = k_{cool} \tag{10}$$
$$\kappa_3 = k_{bisc} \tag{1}$$

For this simple model the following relationship between the species associated spectra, $SAS_i$, and the DADS, $D_i$, is obtained, where $c_0$ is the contribution of the ground state spectrum, $SAS_{S_0}$, and $\Phi_{T_1}$ is the triplet state quantum yield:

$$SAS_{S_1} = \frac{(D_1 + D_2 + D_3)}{c_0} + SAS_{S_0} \tag{2}$$

$$SAS_{T_1^{hot}} = \frac{(\kappa_1 - \kappa_2)D_2 + (\kappa_1 - \kappa_3)D_3}{c_0 \Phi_{T_1} \kappa_1} + SAS_{S_0} \tag{3}$$

$$SAS_{T_1} = \frac{(\kappa_2 - \kappa_3)(\kappa_1 - \kappa_3)D_3}{c_0 \Phi_{T_1} \kappa_1 \kappa_2} + SAS_{S_0} \tag{4}$$

In case the cooling rate constant is in the order of the $S_1$ decay, *i.e.*, $\kappa_1 \approx \kappa_2$, and as $\kappa_1 \approx \kappa_2 \gg \kappa_3$ is given, then $SAS_{T_1^{hot}}$ becomes $SAS_{T_1}$ as observed for complex **1**. In this model the only undetermined parameters are $c_0$ and $\Phi_{T_1}$. By considering the requirement that the resulting SAS must be positive, and should not show any of the characteristic bands of the other species one is able to find at least upper or lower bounds for these values. In particular the negative peaks from the ground state bleach should disappear in the SAS fixing the lower limit. The determination of the individual parameters for each individual case is shown in Figures S3 and S4.
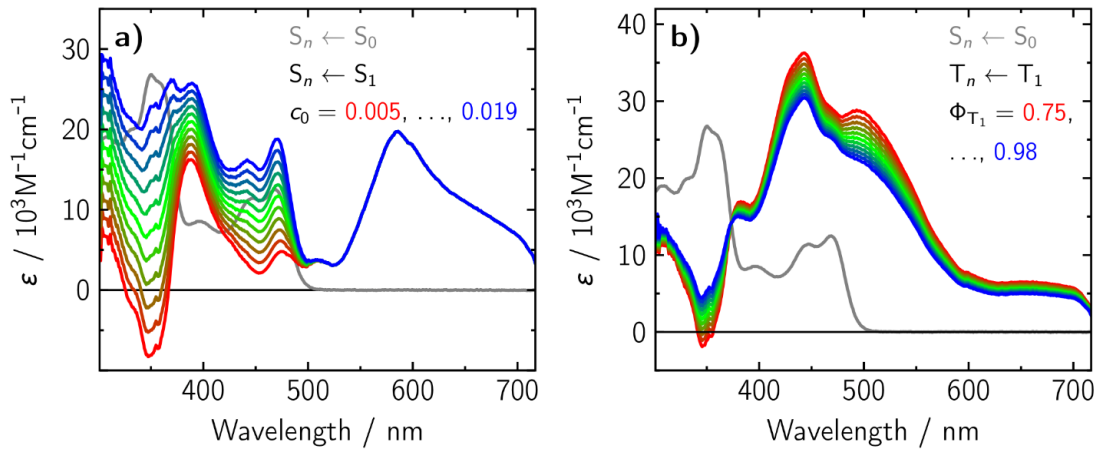
**Figure S3.** SAS of complex **Pt-1** in dcm in the $S_1$ state, $S_n \leftarrow S_1$ transitions, (**a**), and in the $T_1$ state, $T_n \leftarrow T_1$ transitions, (**b**). The contribution of the ground state spectrum, $c_0$, was varied between 0.005 (red) and 0.019 (blue). Below $c_0 = 0.009$ the $S_1$ spectrum becomes negative and above 0.012 the contributions of the $S_0$ spectrum arise. The triplet yield, $\Phi_{T_1}$, was varied between 0.75 (red) and 0.98 (blue). The lower bound for $\Phi_{T_1}$ is 0.80 since below this value the $T_1$ spectrum becomes negative. Since up to $\Phi_{T_1} = 0.98$ the signatures of the $S_0$ spectrum do not start to arise, the preferred value of $\Phi_{T_1}$ is very close to 1.0. The $S_0$ spectrum is also plotted in both panels for comparison.
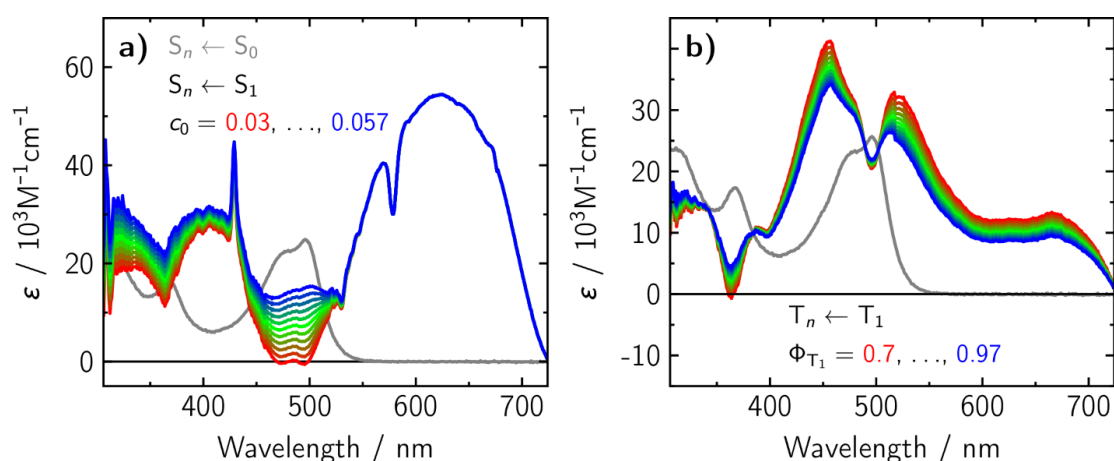


**Figure S4.** SAS of complex **Pt-2** in dcm in the $S_1$ state, $S_n \leftarrow S_1$ transitions, (**a**), and in the relaxed $T_1$ state, $T_n \leftarrow T_1$ transitions, (**b**). The contribution of the ground state spectrum, $c_0$, was varied between 0.03 (red) and 0.057 (blue). Below $c_0 = 0.03$ the $S_1$ spectrum becomes negative and above 0.04 contributions of the $S_0$ spectrum arise. The triplet yield, $\Phi_{T_1}$, was varied between 0.7 (red) and 0.97 (blue). The lower bound for $\Phi_{T_1}$ is 0.72 since below this value the $T_1$ spectrum becomes negative. Since up to $\Phi_{T_1} = 0.97$ the signatures of the $S_0$ spectrum do not start to arise, the preferred value of $\Phi_{T_1}$ is very close to 1.0. The $S_0$ spectrum is also plotted in both panels for comparison.

**Computations.** All calculations were carried out with the Gaussian 09 package[7] utilizing the DFT approach with the M06 functional[8] and the def2-SVP basis set[9] including ECPs for the Pt(II) ion. Geometry optimizations were conducted with "tight" criteria. The C-PCM solvation model[10] applied with solvent parameters for dichloromethane.

**Table S2.** The key structural parameters of complex **Pt-1** derived from single crystal XRD experiment and from DFT optimized ground state ($S_0$) and $T_1$ state geometries. The atom numbering corresponds to that given in Figure 1a.

| Parameter | XRD (esd) | Ground state ($S_0$) | Emitting state ($T_1$) |
|---|---|---|---|
| *Bonds* (Å) | | | |
| Pt-C3 | 1.956(2) | 1.9767 | 1.9504 |
| Pt-N1 | 2.005(2) | 2.0408 | 2.0310 |
| Pt-O1 | 2.0714(16) | 2.1282 | 2.1264 |
| Pt-O2 | 1.9959(19) | 2.0328 | 2.0397 |
| *Angles (degree$^o$)* | | | |
| C3-Pt-N1 | 81.21(10) | 80.743 | 82.380 |
| O1-Pt-O2 | 93.22(10) | 90.867 | 90.985 |
| C3-Pt-O1 | 174.06(10) | 174.536 | 175.326 |
| C3-Pt-O2 | 92.72(10) | 94.591 | 93.688 |
| N1-Pt-O1 | 92.85(7) | 93.799 | 92.947 |
| N1-Pt-O2 | 173.88(7) | 175.332 | 176.068 |
| *Torsion angles (degree$^o$)* | | | |
| C1-N1-Pt-O1 | 178.60(17) | 179.697 | 179.901 |
| C2-C3-Pt-O2 | 177.51(19) | 179.944 | 179.994 |
| C3-C2-C1-N1 | 0.4(3) | 0.106 | 0.007 |
| C4-C5-C6-N2 | 171.63 | 179.709 | 179.911 |
| C2-C3-C4-C5 | 0.1(3) | 0.058 | 0.016 |

**Table S3.** The key structural parameters of complex **Pt-2** derived from single crystal XRD experiment and from DFT optimized ground state ($S_0$) and $T_1$ state geometries. The atom numbering corresponds to that given in Figure 1b.

| Parameter | XRD (esd) | Ground state ($S_0$) | Emitting state ($T_1$) |
|---|---|---|---|
| *Bonds* (Å) | | | |
| Pt1-C3 | 1.981(4) | 1.9855 | 1.9786 |
| Pt1-N1 | 2.002(3) | 2.0374 | 2.0301 |
| Pt1-O1 | 2.069(3) | 2.1297 | 2.1309 |
| Pt1-O2 | 1.998(3) | 2.0337 | 2.0371 |
| Pt2-C4 | 1.986(4) | 1.9855 | 1.9786 |
| Pt2-N2 | 1.995(3) | 2.0374 | 2.0301 |
| Pt2-O3 | 1.992(3) | 2.0337 | 2.0371 |
| Pt2-O4 | 2.077(3) | 2.1297 | 2.1309 |
| *Angles (degree°)* | | | |
| C3-Pt1-N1 | 81.86(15) | 80.749 | 81.755 |
| O1-Pt1-O2 | 92.22(14) | 89.793 | 90.000 |
| C3-Pt1-O1 | 173.64(15) | 174.362 | 174.875 |
| C3-Pt1-O2 | 94.04(15) | 95.802 | 95.124 |
| N1-Pt1-O1 | 91.79(14) | 93.614 | 93.179 |
| N1-Pt1-O2 | 171.98(13) | 170.752 | 172.039 |
| C4-Pt2-N2 | 81.39(15) | 80.749 | 81.755 |
| O3-Pt2-O4 | 91.85(13) | 89.793 | 90.000 |
| C4-Pt2-O3 | 95.59(15) | 95.802 | 95.124 |
| C4-Pt2-O4 | 172.34(15) | 174.362 | 174.875 |
| N2-Pt2-O4 | 91.02(13) | 93.614 | 93.179 |
| N2-Pt2-O3 | 173.63(14) | 170.752 | 172.038 |
| *Torsion angles (degree°)* | | | |
| C1-N1-Pt1-O1 | 169.0(3) | 168.484 | 169.399 |
| C2-C3-Pt1-O2 | 160.9(3) | 158.710 | 159.779 |
| C3-C2-C1-N1 | 4.5(5) | 3.077 | 4.627 |
| C6-N2-Pt2-O4 | 162.3(3) | 168.484 | 169.399 |
| C5-C4-Pt2-O3 | 157.3(3) | 158.710 | 159.780 |
| C4-C5-C6-N2 | 2.9(5) | 3.077 | 4.627 |
| C2-C3-C4-C5 | 5.3(4) | 7.255 | 10.794 |
| Pt1-C3-C4-Pt2 | 11.6(7) | 16.500 | 10.883 |

**Table S4.** DFT calculated frontier orbital energies and atomic contributions of complex **Pt-1** in the $T_1$ state geometry resulting from Mulliken population analysis.

| Orbital | Energy, eV | Contribution, % (Mulliken) | | |
|---|---|---|---|---|
| | | *tfbpH* | *acac* | *Pt* |
| **LUMO+4** | -0.957 | 82 | 15 | 3 |
| **LUMO+3** | -1.087 | 100 | 0 | 0 |
| **LUMO+2** | -1.218 | 18 | 80 | 2 |
| **LUMO+1** | -1.562 | 94 | 3 | 3 |
| **LUMO** | -2.864 | 96 | 1 | 3 |
| **HOMO** | -6.015 | 80 | 3 | 17 |
| **HOMO-1** | -6.591 | 56 | 17 | 28 |
| **HOMO-2** | -6.883 | 7 | 3 | 90 |
| **HOMO-3** | -7.115 | 56 | 7 | 37 |
| **HOMO-4** | -7.496 | 17 | 42 | 41 |

tfbpH – *2,5-bis(5-(trifluoromethyl)pyridin-2-yl)thiophene* residue
acac – acetylacetonate

**Table S5.** DFT calculated frontier orbital energies and atomic contributions of complex **Pt-2** in the state $T_1$ geometry resulting from Mulliken population analysis.

| Orbital | Energy, eV | Contribution, % (Mulliken) | | | | |
|---|---|---|---|---|---|---|
| | | Pt1 | acac1 | tfbp | Pt2 | acac2 |
| **LUMO+4** | -1.105 | 1 | 38 | 21 | 1 | 38 |
| **LUMO+3** | -1.130 | 2 | 42 | 12 | 2 | 42 |
| **LUMO+2** | -1.448 | 0 | 6 | 88 | 0 | 6 |
| **LUMO+1** | -1.682 | 3 | 1 | 92 | 3 | 1 |
| **LUMO** | -2.976 | 3 | 0 | 94 | 3 | 0 |
| **HOMO** | -6.048 | 7 | 1 | 84 | 7 | 1 |
| **HOMO-1** | -6.117 | 20 | 11 | 37 | 20 | 11 |
| **HOMO-2** | -6.574 | 14 | 34 | 5 | 14 | 34 |
| **HOMO-3** | -6.658 | 25 | 18 | 14 | 25 | 18 |
| **HOMO-4** | -6.779 | 43 | 4 | 6 | 43 | 4 |

tfbpH – *2,5-bis(5-(trifluoromethyl)pyridin-2-yl)thiophene* residue
acac1 – acetylacetonate coordinated to Pt1
acac2 – acetylacetonate coordinated to Pt2

**Table S6.** TD-DFT calculated lowest triplet and singlet states of **Pt-1** in the $T_1$ state geometry

| State, energy (eV) | $f$ (oscillator strength) | Contributing transition coefficients* | Character** |
|---|---|---|---|
| *triplets* | | | |
| $T_1$, 1.407 | (triplet) | HOMO→LUMO (0.69) | $LC^{tfbpH}/M^{Pt}L^{tfbpH}CT$ |
| $T_2$, 2.540 | (triplet) | HOMO–1→LUMO (0.55)<br>HOMO–2→LUMO (0.34) | $M^{Pt}L^{tfbpH}CT/L^{acac}L^{tfbpH}CT$ |
| $T_3$, 2.849 | (triplet) | HOMO–3→LUMO (0.47)<br>HOMO–1→LUMO (-0.32) | $M^{Pt}L^{tfbpH}CT/L^{acac}L^{tfbpH}CT/\ LC^{tfbpH}$ |
| $T_4$, 3.074 | (triplet) | HOMO→LUMO+1 (0.61)<br>HOMO–3→LUMO (-0.28) | $LC^{tfbpH}/M^{Pt}L^{tfbpH}CT$ |
| $T_5$, 3.282 | (triplet) | HOMO–1→LUMO+2 (0.39)<br>HOMO→LUMO+2 (0.28)<br>HOMO–7→LUMO (-0.24)<br>HOMO→LUMO+4 (-0.21) | $LC^{tfbpH}/M^{Pt}L^{tfbpH}CT/\ L^{acac}L^{tfbpH}CT$ |
| *singlets* | | | |
| $S_1$, 2.387 | 0.4258 | HOMO→LUMO (0.69) | $LC^{tfbpH}/M^{Pt}L^{tfbpH}CT$ |
| $S_2$, 2.932 | 0.0037 | HOMO–2→LUMO (0.70) | $M^{Pt}L^{tfbpH}CT$ |
| $S_3$, 2.965 | 0.1324 | HOMO–1→LUMO (0.69) | $M^{Pt}L^{tfbpH}CT/L^{acac}L^{tfbpH}CT$ |
| $S_4$, 3.369 | 0.5394 | HOMO–3→LUMO (0.68) | $LC^{tfbpH}/M^{Pt}L^{tfbpH}CT$ |
| $S_5$, 3.476 | 0.1045 | HOMO→LUMO+1 (0.67) | $M^{Pt}L^{tfbpH}CT/L^{acac}L^{tfbpH}CT/\ LC^{tfbpH}$ |

*Square of the coefficient multiplied by two gives percentage contribution of the transition to formation of the excited state.

**MLCT – Metal (M) to Ligand (L) Charge Transfer. LC-Ligand Centered. LLCT – Ligand to Ligand Charge Transfer.

**Table S7.** TD-DFT calculated lowest triplet and singlet states of **Pt-2** in the $T_1$ state geometry

| State, energy (eV) | $f$ (oscillator strength) | Contributing transition coefficients* | Character** |
|---|---|---|---|
| *triplets* | | | |
| $T_1$, 1.372 | (triplet) | HOMO→LUMO (0.70) | $LC^{tfbp}/M^{Pt}L^{tfbp}CT$ |
| $T_2$, 1.846 | (triplet) | HOMO−3→LUMO (0.15) HOMO−1→LUMO (0.67) | $M^{Pt}L^{tfbp}CT/L^{acac}L^{tfbp}CT/LC^{tfbp}$ |
| $T_3$, 2.612 | (triplet) | HOMO−3→LUMO (0.62) HOMO−8→LUMO (-0.17) HOMO−1→LUMO (-0.15) | $M^{Pt}L^{tfbp}CT/ L^{acac}L^{tfbp}CT/LC^{tfbp}$ |
| $T_4$, 2.636 | (triplet) | HOMO−2→LUMO (0.63) HOMO−4→LUMO (0.14) HOMO−6→LUMO (-0.16) | $M^{Pt}L^{tfbp}CT/ L^{acac}L^{tfbp}CT/LC^{tfbp}$ |
| $T_5$, 2.680 | (triplet) | HOMO−5→LUMO (0.67) HOMO−3→LUMO (0.14) | $M^{Pt}L^{tfbp}CT/ LC^{tfbp}$ |
| *singlets* | | | |
| $S_1$, 2.309 | 0.5055 | HOMO→LUMO (0.69) | $LC^{tfbp}/M^{Pt}L^{tfbp}CT$ |
| $S_2$, 2.325 | 0.0931 | HOMO−1→LUMO (0.68) HOMO−3→LUMO (0.17) | $M^{Pt}L^{tfbp}CT/L^{acac}L^{tfbp}CT /LC^{tfbp}$ |
| $S_3$, 2.724 | 0.0135 | HOMO−3→LUMO (0.49) HOMO−5→LUMO (0.47) | $M^{Pt}L^{tfbp}CT/L^{acac}L^{tfbp}CT$ |
| $S_4$, 2.737 | 0.0074 | HOMO−4→LUMO (0.68) HOMO−2→LUMO (0.16) | $M^{Pt}L^{tfbp}CT/L^{acac}L^{tfbp}CT$ |
| $S_5$, 2.844 | 0.0135 | HOMO−2→LUMO (0.67) HOMO−4→LUMO (-0.16) | $M^{Pt}L^{tfbp}CT/L^{acac}L^{tfbp}CT$ |

*Square of the coefficient multiplied by two gives percentage contribution of the transition to formation of the excited state.

**MLCT – Metal (M) to Ligand (L) Charge Transfer. LC-Ligand Centered. LLCT – Ligand to Ligand Charge Transfer.

## Biological studies

**Cell viability assay.** Inhibition of host cells' viability by tested compound was detected using MTT reduction assay. Murine fibroblast cells L929 (ATTC® catalog no. CCL-1™, recommended by the International Standard ISO 10993:2009 for evaluation of cytotoxic activities of new compounds) and human HeLa cells (ATTC® catalog no. CCL-2™) were seeded on 96-well microplates at a density of 1 x $10^4$ cells per well and cultivated in Dulbecco's Modified Eagle's Medium (DMEM, Biowest) supplemented with 10% fetal bovine serum (FBS, Biowest), 100 U mL$^{-1}$ of penicillin, and 100 μg mL$^{-1}$ of streptomycin (Biowest). After overnight incubation at 37˚C and 5% $CO_2$, the growth medium was removed and 100 mL

of fresh medium supplemented with compound in the concentration range of 0.15–10 µM. The tested compound was dissolved in DMSO, with final concentration in the medium not exceeding 1%. Cells were further incubated for 72 h with tested agent and then 50 µg MTT per well was added (Sigma-Aldrich), and plates were incubated for the next 2 h at 37˚C. Formazan crystals were solubilized in 150 mL DMSO and quantified by spectrophotometric measurement at 570 nm using the SpectraMax i3 Multi-Mode Platform (Molecular Devices). In addition, in order to select the appropriate conditions for microscopic examination, the toxicity of **Pt-1** at a concentration of 10 µM after 24 h of incubation with cells was determined. The results of the experiments were presented as mean arithmetic values from three repeats in each of two independent experiments and the percentage of viability inhibition was calculated in comparison with the untreated controls. $IC_{50}$ values (drug concentration that inhibits the cell viability by 50%) were calculated with the Prism GraphPad 7 software using nonlinear regression.

**Confocal microscopy.** Human HeLa cells (ATTC® - CCL-2™) were cultured for 24 h after seeding on a chambered coverslip with 4 wells (ibidi, cat. no: 80426), reaching approximately 50% confluency. The cells were grown in RPMI 1640 medium without phenol red (Biowest) supplemented with 10% fetal bovine serum (FBS, Biowest) at 5% $CO_2$ and 37°C. Subsequently, the medium was changed and cells were incubated with fresh medium containing 10 µM of **Pt-1** for 5 h prior to imaging. Fluorescence imaging of live HeLa cells with **Pt-1** complex was performed using DMI 6000 CS inverted microscope with TCS SP8 confocal system operated by LAS 2.0.2.15022 software (Leica Microsystem, Wetzlar, Germany). The observations were made using HC PLAPO CS2 63x/1.40 oil immersion objective. The parameters of the excitation and the emission were unified for the control material and that stained with tested compound. The excitation and detection were made sequentially for "green" (450-560 nm) and "red" (680-780 nm) signal and UV diode laser (405 nm, 5 mW nominal power with 5% and 7% intensity, respectively) was used for **Pt-1** excitation. The emission was collected at the range of 450-560 nm by the hybrid detector (HyD) in standard mode (gain 100%, offset 0%) and at the range of 680-780 nm by the hybrid detector (HyD) in bright R mode (gain 150%, offset 0%). Additionally, transmitted light was also collected by the conventional detector-photomultiplier tube (PMT). Confocal scans were performed bidirectionally at 600 Hz speed for the single image and for the Z-stack scans with 600 Hz speed to prevent fotobleaching, line average was set at 3. The fluorescence was registered from the single confocal section (pinhole 1.0 Airy unit). Image logical size was 512 × 512 (Physical length 67.34 µm × 67.34 µm = 0.132 µm × 0.132 µm Pixel size/Voxel size). The 3D visualization of the green and red emission in HeLa cells was carried out. The Z-stack scans were performed every 0.3 nm and 3D images were analyzed to countercheck the presence of the assayed complex in the cytoplasm and nucleus.
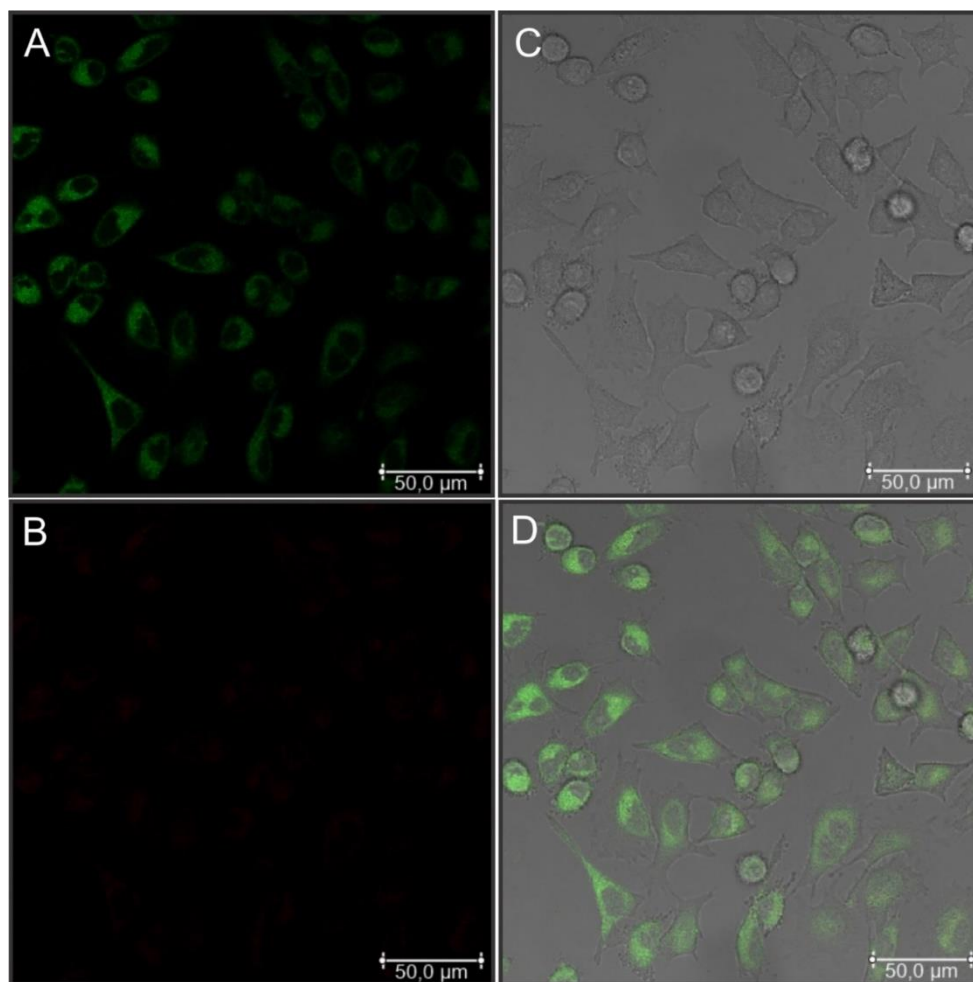
**Figure S5.** Confocal luminescence image of HeLa cells stained with complex **Pt-1**; (A) detection at 450-560 nm; (B) detection at 680-780 nm; (C) transmitted light; (D) merged image of (A), (B) and transmitted light. Image logical size 512 x 512 (Physical length 246.03 μm x 246.03 μm = Pixel size/Voxel size 0.481 μm x 0.481 μm).
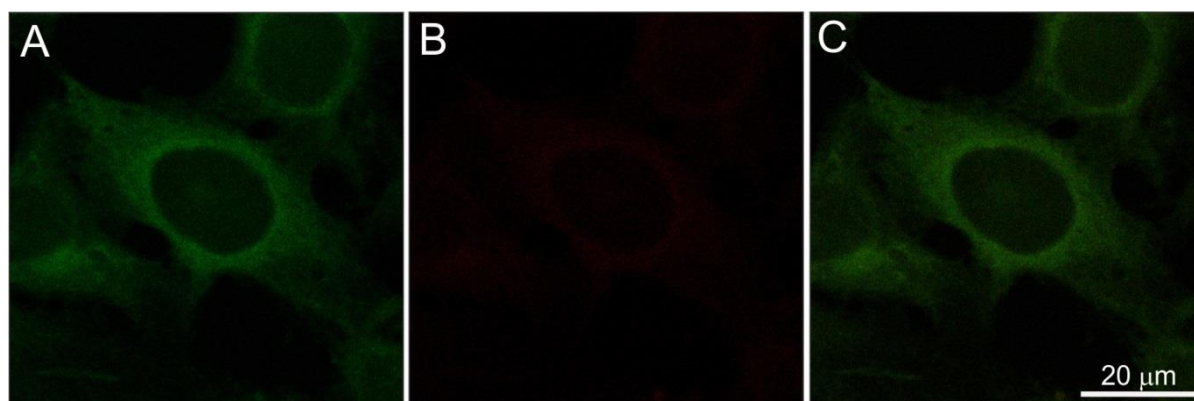


**Figure S6.** Confocal luminescence images of HeLa cells stained with complex **Pt-1**; (A) detection at 450-560 nm; (B) detection at 680-780 nm; (C) merged image of (A) and (B)

**References**

1. G. Sheldrick, *Acta Cryst. A*, 2015, **71**, 3-8.
2. O. V. Dolomanov, L. J. Bourhis, R. J. Gildea, J. A. K. Howard and H. Puschmann, *J. Appl. Cryst.*, 2009, **42**, 339-341.
3. A. A. Gorman, I. Hamblett, C. Lambert, A. L. Prescott, M. A. J. Rodgers and H. M. Spence, *J. Am. Chem. Soc.*, 1987, **109**, 3091-3097.
4. C. Martí, O. Jürgens, O. Cuenca, M. Casals and S. Nonell, *J. Photochem. Photobiol. A*, 1996, **97**, 11-18.
5. R.-J. Kutta, T. Langenbacher, U. Kensy and B. Dick, *Appl. Phys. B*, 2013, **111**, 203-216.
6. R.-J. Kutta, U. Kensy and B. Dick, in *Chemical Photocatalysis*, ed. B. König, De Gruyter, Leipzig, 2013, pp. 295–318.
7. M. J. Frisch, G. W. Trucks, H. B. Schlegel, G. E. Scuseria, M. A. Robb, J. R. Cheeseman, G. Scalmani, V. Barone, B. Mennucci, G. A. Petersson, et al., *Gaussian 09*, Gaussian, Inc., Wallingford, CT, USA, 2009.
8. Y. Zhao and D. G. Truhlar, *Theor. Chem. Acc.*, 2008, **120**, 215-241.
9. F. Weigend and R. Ahlrichs, *Phys. Chem. Chem. Phys.*, 2005, **7**, 3297-3305.
10. M. Cossi, N. Rega, G. Scalmani and V. Barone, *J. Comput. Chem.*, 2003, **24**, 669-681.